AGU PUBLICATIONS

JGR

Journal of Geophysical Research: Solid Earth

RESEARCH ARTICLE

10.1002/2013JB010567

Key Points:
- Wave-induced fluid flow effects in fractured rocks are numerically simulated
- Strong changes in *P* wave properties due to fracture connectivity are observed
- Seismic data are expected to contain key hydraulic information of fractured rocks

Correspondence to:
J. Germán Rubino,
German.Rubino@unil.ch

Citation:
Rubino, J. G., T. M. Müller, L. Guarracino, M. Milani, and K. Holliger (2014), Seismoacoustic signatures of fracture connectivity, *J. Geophys. Res. Solid Earth*, *119*, 2252–2271, doi:10.1002/2013JB010567.

Received 29 JUL 2013
Accepted 11 FEB 2014
Accepted article online 15 FEB 2014
Published online 31 MAR 2014

Seismoacoustic signatures of fracture connectivity

J. Germán Rubino[1], Tobias M. Müller[2], Luis Guarracino[3], Marco Milani[1], and Klaus Holliger[1]

[1]Applied and Environmental Geophysics Group, University of Lausanne, Lausanne, Switzerland, [2]Earth Science and Resource Engineering Division, Commonwealth Scientific and Industrial Research Organization, Perth, Western Australia, Australia, [3]CONICET, Facultad de Ciencias Astronúmicas y Geofúsicas, Universidad Nacional de La Plata, La Plata, Argentina

Abstract Wave-induced fluid flow (WIFF) between fractures and the embedding matrix as well as within connected fractures tends to produce significant seismic attenuation and velocity dispersion. While WIFF between fractures and matrix is well understood, the corresponding effects related to fracture connectivity and the characteristics of the energy dissipation due to flow within fractures are largely unexplored. In this work, we use oscillatory relaxation simulations based on the quasi-static poroelastic equations to study these phenomena. We first consider synthetic rock samples containing connected and unconnected fractures and compute the corresponding attenuation and phase velocity. We also determine the relative fluid displacement and pressure fields in order to gain insight into the physical processes involved in the two manifestations of WIFF in fractured media. To quantify the contributions of the two WIFF mechanisms to the total seismic attenuation, we compute the spatial distribution of the local energy dissipation. Finally, we perform an exhaustive sensitivity analysis to study the role played by different characteristics of fracture networks on the seismic signatures. We show that in the presence of connected fractures both *P* wave attenuation and phase velocity are sensitive to some key characteristics of the probed medium, notably to the lengths, permeabilities, and intersection angles of the fractures as well as to the overall degree of connectivity of the fracture network. This, in turn, indicates that a deeper understanding of these two manifestations of WIFF in fractured media may eventually allow for the extraction of some of these properties from seismic data.

1. Introduction

The presence of fractures is very common in most geological formations and tends to dominate their mechanical and hydraulic properties. This is why there is great interest in improving techniques to detect and characterize fracture networks. The range of potential applications spans multiple domains throughout the Earth, environmental, and engineering sciences, including groundwater and contaminant hydrology, nuclear waste storage, CO_2 sequestration, hydrocarbon exploration and production, and tunnel engineering, among many others [e.g., *Liu et al.*, 2000; *Nelson*, 2001; *Maultzsch et al.*, 2003].

The analysis of fractures through direct observations is generally difficult due to the limited sampling of the affected rock volumes and hence remote-sensing-type approaches are of significant interest. Seismic methods are particularly valuable for the noninvasive detection and characterization of fractures [e.g., *Maultzsch et al.*, 2003; *Clark et al.*, 2009]. Since in most cases the resolution of seismic data is insufficient for directly imaging fractures, most of the related research efforts focus on seismic attribute analysis [e.g., *Bakulin et al.*, 2000]. Correspondingly, various seismic attributes, such as shear wave splitting and azimuthal variations in *P* wave attenuation and phase velocity, have been identified as diagnostic features that may permit to estimate some key properties of fractured media, including the density, the average length, and the orientation of the fractures [e.g., *Liu et al.*, 2000; *Maultzsch et al.*, 2003; *Liu et al.*, 2007; *Clark et al.*, 2009; *Schijns et al.*, 2012]. Notably, seismic attenuation has been recognized as a potentially important parameter for this purpose, since different studies have shown that seismic energy loss is very significant in fractured rock masses and tends to increase with increasing fracture density [e.g., *Peacock et al.*, 1994; *Maultzsch et al.*, 2003; *Payne et al.*, 2007; *Clark et al.*, 2009; *Varghese et al.*, 2009].

Until recently, the elevated seismic attenuation levels observed in fractured rocks had been considered to be mainly produced by wave-induced fluid flow (WIFF) between the fractures and the pore space of the embedding matrix [e.g., *Peacock et al.*, 1994; *Chapman*, 2003; *Brajanovski et al.*, 2005; *Chapman*, 2009; *Gurevich et al.*, 2009]. That is, due to the very high compressibility contrast between the fractures and the

porous background, seismic waves induce strong fluid pressure gradients and associated fluid flow between such regions, which in turn produces significant energy dissipation [e.g., *Brajanovski et al.*, 2005; *Gurevich et al.*, 2009; *Müller et al.*, 2010]. As the wave-induced fluid pressure equilibration process is governed by the hydraulic properties of the fractured rock sample, one should expect that the resulting seismic attenuation also contains information about fracture connectivity. Recently, *Rubino et al.* [2013] have indeed identified an additional and as of yet unknown manifestation of WIFF in the presence of fracture connectivity, which is related to fluid flow within the connected fractures. The results of this pilot study indicate that this additional energy loss mechanism can be very important and that the presence of connected fractures can also affect the attenuation levels due to WIFF between fractures and the embedding matrix.

Since fracture connectivity controls the flow and transport properties of fractured formations [e.g., *Berkowitz et al.*, 2000], the findings of *Rubino et al.* [2013] are of significant importance, as a better understanding of the role played by fracture connectivity on the behavior of seismic waves may help to extract key hydraulic information from seismic data. These results could find direct applications in the seismic monitoring of systems for which changes in fracture connectivity are of interest. An example of a potential application could be in seismic monitoring of volcanoes. Indeed, an eruption can take place only if the magma body finds or creates a network of connected fractures to reach the surface. Though some of the fractures may already exist, others still have to be created as the magma pushes to find a path to flow [e.g., *Kilburn*, 2003]. Interestingly, the same kind of information may also be of relevance in seismically active zones, as fracture connectivity is considered to play a major role in the generation of earthquakes [e.g., *Hardebeck and Hauksson*, 1999]. Another domain where fracture connectivity is a key parameter is modern shale gas and oil exploitation. In this case, the hydrocarbons are located in the tight pore space of reservoirs characterized by extremely low natural permeability, and therefore, hydraulic fracturing is needed to extract them. Fluid flow then takes place almost exclusively in the artificially generated fractures, and hence, the information related to fracture connectivity potentially contained in seismic data may turn out to be very valuable. The same applies for most deep geothermal reservoirs, where hydraulic fracturing is also needed to allow for fluid circulation and heat extraction [e.g., *Legarth et al.*, 2005].

In this work, we seek to extend and complement the initial research of *Rubino et al.* [2013] by performing an exhaustive sensitivity analysis of seismic attenuation and velocity dispersion due to WIFF within fractures. The main objective is to understand in more detail this recently identified manifestation of WIFF, notably with regard to the roles played by various key properties of the probed material, such as the lengths, permeabilities, and intersection angles of the fractures. Particular attention is paid to the spatial distribution of energy dissipation within the considered fractured rocks, which yields further insight into this new manifestation of WIFF. Finally, we also explore the global effect of WIFF for fracture networks characterized by varying degrees of interconnectivity.

2. Characteristic Scales of WIFF

WIFF can arise in the presence of heterogeneities in the mesoscopic scale range. This means that the characteristic length scale of the heterogeneities a_{meso} satisfies

$$a_{\text{pore}} \ll a_{\text{meso}} \ll \lambda, \tag{1}$$

where a_{pore} denotes the typical pore or grain size and λ the dominant seismic wavelength. The propagation of seismic waves through a medium containing mesoscopic heterogeneities produces local fluid pressure gradients, which are equilibrated through pressure diffusion and thus result in seismic energy dissipation. The magnitude of the associated seismic attenuation scales with the compressibility contrast between the heterogeneities and their embedding background [*Pride et al.*, 2004]. Please note that there is no net fluid flow associated with WIFF, that is, the total amount of fluid mass contained in the pore space of any sample before and after the passing of a seismic perturbation remains constant.

The seismic response of fractured rocks can be modeled in the framework of *Biot* [1962] theory of poroelasticity with the mesoscopic fractures represented as highly compliant and permeable heterogeneities embedded in a stiffer porous matrix [*Brajanovski et al.*, 2005; *Gurevich et al.*, 2009]. This means that the fractures are part of the poroelastic continuum. The porosity of the background material is referred to as the equant porosity and is assumed to be hydraulically connected with the fracture porosity. As fractures are very compliant, the compressibility contrast with regard to the background material is large, and hence,

WIFF can be important in fractured rocks [e.g., *Pride et al.*, 2004]. Therefore, when a seismic wave is incident on a mesoscopic fracture, an oscillatory fluid flow is induced from the fracture into the equant pore space and vice versa. For the following, we refer to this manifestation of WIFF as the fracture-background WIFF, or briefly, FB-WIFF. The relevant spatial scale for this FB-WIFF is the diffusion length

$$L_{\mathrm{d}}^{\mathrm{b}} \equiv \sqrt{D^{\mathrm{b}}/\omega}, \tag{2}$$

where ω is the angular frequency of the seismic wave and D^{b} is the pressure diffusivity of the background material. This diffusivity can be expressed in terms of the poroelastic properties of the fluid-saturated porous rock [e.g., *Rubino et al.*, 2012]

$$D^{\mathrm{b}} = \frac{\kappa^{\mathrm{b}}}{\eta}\left(\frac{H^{\mathrm{b}}M^{\mathrm{b}} - (\alpha^{\mathrm{b}}M^{\mathrm{b}})^2}{H^{\mathrm{b}}}\right), \tag{3}$$

where κ^{b} and η denote the permeability of the background material and the shear viscosity of the fluid, respectively. The additional parameters in equation (3) are given by [e.g., *Rubino et al.*, 2012]

$$\alpha^{\mathrm{b}} = 1 - \frac{K_m^{\mathrm{b}}}{K_s^{\mathrm{b}}}, \tag{4}$$

$$M^{\mathrm{b}} = \left(\frac{\alpha^{\mathrm{b}} - \phi^{\mathrm{b}}}{K_s^{\mathrm{b}}} + \frac{\phi^{\mathrm{b}}}{K_f}\right)^{-1}, \tag{5}$$

$$H^{\mathrm{b}} = K_m^{\mathrm{b}} + \frac{4}{3}\mu_m^{\mathrm{b}} + \left(\alpha^{\mathrm{b}}\right)^2 M^{\mathrm{b}}, \tag{6}$$

where K_s^{b} and K_m^{b} denote the bulk moduli of the solid grains and of the dry matrix of the background material, K_f the bulk modulus of the pore fluid, μ_m^{b} the shear modulus of the dry frame, and ϕ^{b} the porosity of the background rock.

The fluid pressure relaxation is governed by fluid pressure diffusion with a characteristic transition frequency ω_c^{b}. At this frequency, the diffusion length $L_{\mathrm{d}}^{\mathrm{b}}$ is of similar size as the characteristic size of the background material lying between consecutive fractures, a_{meso}, so that

$$\omega_c^{\mathrm{b}} \approx D^{\mathrm{b}}/a_{\mathrm{meso}}^2. \tag{7}$$

For frequencies $\omega \ll \omega_c^{\mathrm{b}}$ the diffusion lengths are much larger than the typical size of the heterogeneities. Correspondingly, there is enough time during each oscillatory half-cycle for the pore fluid pressures of fractures and background to equilibrate. Conversely, for frequencies $\omega \gg \omega_c^{\mathrm{b}}$ the diffusion lengths are very small compared to the size of the background material, and hence, there is no time for communication between the pore fluid of the fractures and that of the equant pore space. In this case, the pore pressure is approximately constant within each region. For intermediate frequencies, as characterized by diffusion lengths that are comparable to the characteristic size of the material lying between consecutive fractures, that is, frequencies ω close to ω_c^{b}, significant pressure gradients and fluid flow between the fractures and the background can be induced by the seismic wave. This in turn results in attenuation and velocity dispersion. Correspondingly, the characteristic transition frequency ω_c^b is also associated with maximum FB-WIFF attenuation.

From equations (3) and (7), we see that the frequency range where this energy dissipation operates shifts toward lower frequencies for decreasing background permeability and increasing characteristic size of the background material or, equivalently, increasing spacing between fractures. However, for FB-WIFF, the properties of the fracture material do not affect the location of the attenuation peak.

Rubino et al. [2013] recently showed that, apart from the energy dissipation due to FB-WIFF, another manifestation of WIFF exists in the presence of connected fractures. The corresponding seismic energy dissipation is governed by pressure diffusion within interconnected fractures: fractures oriented quasiperpendicularly to the direction of propagation of a *P* wave experience a fluid pressure increase (or decrease) in response to the stresses applied by the perturbation, and therefore, fluid is injected into (or withdrawn from) the connected fractures. For the following, we refer to this mechanism as fracture-fracture WIFF or, briefly, FF-WIFF. If the permeability of the background material is much smaller than that of the fractures, which is the most typical situation, then it can be neglected from a hydraulic point of view. Correspondingly,

the location of the FF-WIFF attenuation peak is determined by the frequency at which the diffusion length in the fracture material is of similar size as the characteristic length of the fractures. That is, the transition frequency of FF-WIFF is given by

$$\omega_c^{\mathrm{f}} \approx D^{\mathrm{f}}/a_{\mathrm{f}}^2, \tag{8}$$

where D^{f} is the pressure diffusivity of the fracture material and a_{f} characterizes the lengths of the fractures. It is interesting to notice here that, contrary to FB-WIFF attenuation, the location of the FF-WIFF attenuation peak is expected to contain information on the defining properties of the fractures per se, such as their permeabilities and characteristic lengths.

In the following, we shall analyze WIFF effects in fractured media through the use of numerical oscillatory relaxation tests based on the equations of quasi-static poroelasticity. The corresponding methodological foundations and the numerical implementation are outlined in Appendix A.

3. Results

In this section, we complement and extend the initial analysis presented by *Rubino et al.* [2013] to study in more detail the newly discovered FF-WIFF. For the following, it is important to point out that we have performed an exhaustive convergence analysis to make sure that the employed grid spacing is small enough to properly represent the diffusion processes associated with FB-WIFF and FF-WIFF.

3.1. Material Properties and Fracture Parameterization

We consider a poroelastic model corresponding to a sandstone containing a set of mesoscopic fractures. The fractures and the equant pore space are fully saturated with water, which has a bulk modulus K_f of 2.25 GPa, a density ρ_f of 1.09 g/cc, and a shear viscosity η of 0.001 Pa s.

For the sandstone representing the background material we consider a porosity ϕ^{b} of 0.1 and for the solid grains composing this region we use the properties of quartz, that is, a bulk modulus K_s^{b} of 37 GPa, a shear modulus μ_s^{b} of 44 GPa, and a density ρ_s^{b} of 2.65 g/cc. To link the porosity ϕ^{b} and the solid grain properties with the elastic moduli of the dry frame, we use the empirical model of *Krief et al.* [1990]

$$K_m^{\mathrm{b}} = K_s^{\mathrm{b}}(1-\phi^{\mathrm{b}})^{3/(1-\phi^{\mathrm{b}})}, \tag{9}$$

$$\mu_m^{\mathrm{b}} = K_m^{\mathrm{b}}\mu_s^{\mathrm{b}}/K_s^{\mathrm{b}}. \tag{10}$$

This yields $K_m^{\mathrm{b}} = 26$ GPa and $\mu_m^{\mathrm{b}} = 31$ GPa for the drained-frame bulk and shear moduli, respectively. In order to separate the attenuation peak corresponding to FB-WIFF from that due to FF-WIFF, we consider a very low permeability for the background material ($\kappa^{\mathrm{b}} = 10^{-2}$ mD).

We assume that, at the grain level, the solid material properties of the fractures are the same as those of the embedding matrix. Following *Nakagawa and Schoenberg* [2007], we characterize the elastic properties of the drained fracture in terms of the shear and drained normal compliances

$$\eta_T = h/\mu_m^{\mathrm{f}}, \tag{11}$$

$$\eta_N = h/(K_m^{\mathrm{f}} + \frac{4}{3}\mu_m^{\mathrm{f}}), \tag{12}$$

where K_m^{f} and μ_m^{f} are the drained-frame bulk and shear moduli of the fracture and h its aperture.

For the following, we consider two quasi-orthogonal fractures without and with intersection (Figure 1). The rock sample is a square of side length 3.33 cm and the mean aperture of the fractures h is 0.033 cm. Using $\eta_T = 3 \times 10^{-11}$ m/Pa and $\eta_N = 10^{-11}$ m/Pa as proposed by *Nakagawa and Schoenberg* [2007], we obtain $K_m^{\mathrm{f}} = 0.02$ GPa and $\mu_m^{\mathrm{f}} = 0.01$ GPa. We assume for the porous material composing the fractures a porosity ϕ^{f} of 0.5 and a permeability κ^{f} of 100 D.

Please note that, unless explicitly mentioned otherwise, we use the parameterization and rock physical properties outlined above for the numerical simulations presented in this work.

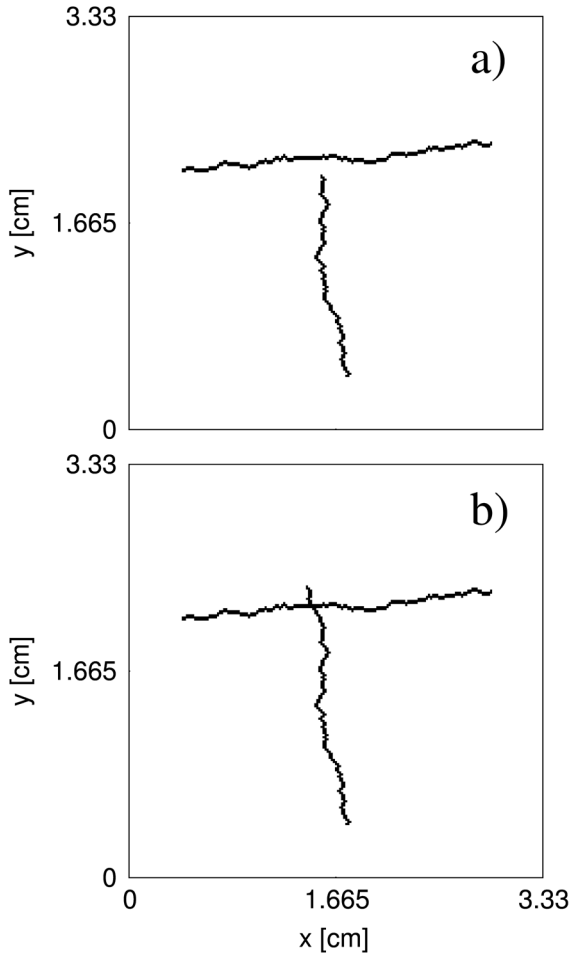

Figure 1. Synthetic rock samples employed to analyze fracture connectivity effects on *P* wave attenuation. Fractures are denoted by solid "wiggly" lines. (a and b) Samples contain two quasi-orthogonal mesoscopic fractures without and with intersection, respectively.

3.2. Manifestation of WIFF Due to Fracture Connectivity – FF-WIFF

Figure 2 shows the inverse quality factor Q_p^{-1} and the phase velocity V_p for vertically incident *P* waves as functions of frequency for the two samples shown in Figure 1. The red curve in Figure 2a shows that the presence of fractures perpendicular to the direction of wave propagation produces considerable attenuation, with Q_p values below 25 over a wide-frequency range. This is expected, because the strong compressibility contrast between the quasi-horizontal fracture and background material produces a large amount of fluid flow between these two media in response to the applied strains. In agreement with the Kramers-Kronig relations [e.g., *Mavko et al.*, 2009], the high attenuation levels produced by the quasi-horizontal fracture (Figure 2a) are also associated with strong velocity dispersion effects over a wide-frequency range (Figure 2b).

By comparing the blue and red curves, we see that when the fractures intersect, significant changes in the overall attenuation and in the phase velocity behavior arise. In particular, the attenuation level corresponding to FB-WIFF decreases and a second attenuation peak arises at higher frequencies. The latter is due to FF-WIFF [*Rubino et al.*, 2013]. It is interesting to note that even though the FF-WIFF attenuation peak is located outside the seismic frequency band, the presence of connected fractures also affects the behavior of the FB-WIFF attenuation peak, as can be seen in Figure 2a. This means that even in those unfavorable cases, seismic attenuation and phase velocity may encode some information on fracture connectivity. In agreement with the attenuation behavior, the frequency range where velocity dispersion is significant gets much broader in the connected scenario (Figure 2b), which in turn demonstrates that phase velocity also contains valuable information with regard to the connectivity of the fractures.

To explore the asymptotic behaviors of the attenuation peak due to FF-WIFF, we include in Figure 3, a log-log plot of the inverse quality factor as a function of frequency for the sample shown in Figure 1b. For this particular analysis, we reduce the permeability of the background material to $\kappa^b = 10^{-5}$ mD in order to separate the two attenuation peaks even more. We observe that the attenuation peak due to FF-WIFF contains two asymptotic regimes, where $1/Q_p$ is proportional to ω and $\omega^{-1/2}$. These two regimes are separated by the transition frequency $\omega_c^f/2\pi$. It is interesting to notice that, in the case of FB-WIFF in a periodic medium, three distinct frequency regimes exist. This is expected as two very different length scales are involved in this case: the fracture thickness and the separation between consecutive horizontal fractures [*Gurevich et al.*, 2009]. However, while the low- and high-frequency asymptotes are in good agreement with those observed by *Gurevich et al.* [2009], the intermediate frequency regime explored by these authors, where $1/Q_p$ is proportional to $\omega^{1/2}$, is absent in Figure 3. This may be due to the fact that the intermediate regime observed by *Gurevich et al.* [2009] corresponds to a periodic 1-D distribution of fractures. In our case, the presence of the

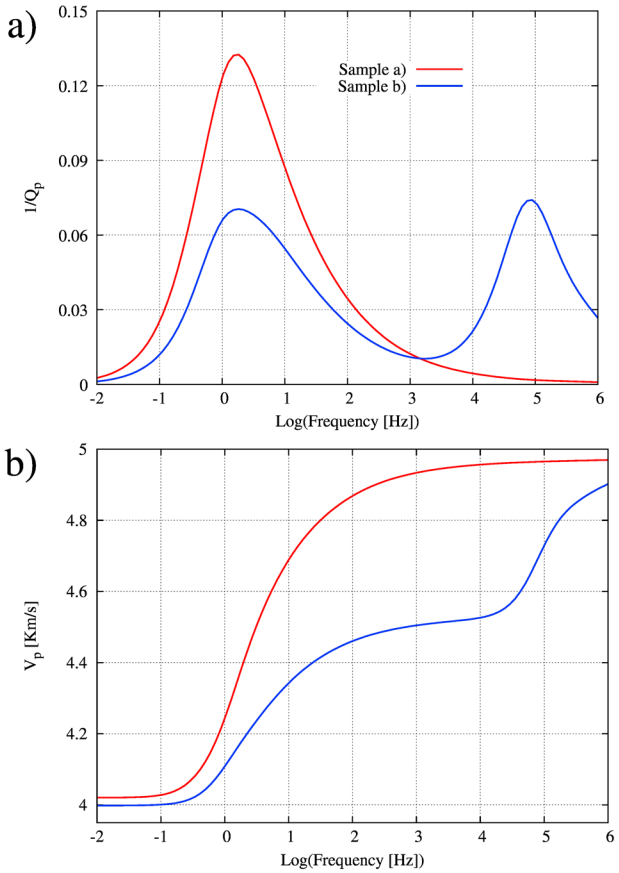

Figure 2. (a) Inverse quality factor and (b) phase velocity for vertically propagating *P* waves as functions of frequency for the samples shown in Figure 1.

quasi-vertical fracture breaks this symmetry and discrepancies with respect to the behavior observed by *Gurevich et al.* [2009] arise.

In order to analyze the physical nature of the attenuation peaks, we calculate the pertinent poroelastic fields. Figure 4 shows the real part of the fluid pressure field corresponding to a vertical displacement imposed at the top boundary of the sample of amplitude 3.33×10^{-9} m, that is, corresponding to an overall vertical strain amplitude of 10^{-7}. Figures 5 and 6 show the vertical and horizontal components of the real part of the relative fluid displacement normalized with respect to the amplitude of the vertical displacement imposed at the top boundary of the sample, respectively. Figures 4a, 4b, 5a, 5b, 6a, and 6b correspond to the sample shown in Figure 1a, whereas Figures 4c, 4d, 5c, 5d, 6c, and 6d correspond to the sample shown in Figure 1b. Please also note that these fields are computed at the frequencies of the two local attenuation maxima, that is, at 1.7 Hz (Figures 4a, 4c, 5a, 5c, 6a, and 6c) and 82.5 kHz (Figures 4b, 4d, 5b, 5d, 6b, and 6d).

For the frequency at which the first attenuation peak occurs, Figure 4a shows a significant fluid pressure increase in the highly compliant quasi-horizontal fracture as compared to the stiffer background in response to the applied strain. The resulting fluid pressure gradient induces significant FB-WIFF, as can be seen in Figure 5a. The attenuation related to FB-WIFF is quantified by the red curve in Figure 2a. Even though there is no connection between the two fractures, a nonnegligible amount of fluid flow occurs inside both the quasi-horizontal and quasi-vertical fractures (Figures 5a and 6a). This is due to the very high permeability of the fracture material, which, as stipulated by equation (A2), leads to significant fluid flow in response to a slight fluid pressure gradient. In the case of the quasi-vertical fracture, the distance between its upper tip and the quasi-horizontal fracture is smaller than the diffusion length in the background material, and therefore, the fluid pressure diffused from the quasi-horizontal fracture manages to reach the quasi-vertical fracture. This in turn creates a rather small fluid pressure gradient and corresponding fluid flow inside the quasi-vertical fracture. As we will show later, the contribution of fluid flow inside the fractures to the total attenuation is, however, rather negligible in this case.

It is also interesting to notice that the fluid pressure induced within the quasi-vertical fracture is relatively low so that its presence does not change significantly the overall fluid pressure field throughout the sample. However, when the quasi-vertical fracture intersects the quasi-horizontal one, the fluid pressure field changes rather dramatically, as can be seen in Figure 4c. We observe that the fluid pressure in the quasi-vertical fracture increases significantly while the quasi-horizontal fracture experiences a fluid pressure reduction as compared to the unconnected scenario (compare Figures 4a and 4c). This altered pressure distribution is due to the hydraulic connectivity between the two fractures. Correspondingly, the amount of fluid flowing between the quasi-horizontal fracture and the background rock decreases, as illustrated by a comparison of Figures 5a and 5c. However, as shown in Figures 5c and 6c, FB-WIFF also takes place in the vicinity of the quasi-vertical fracture, albeit at a less significant level. In addition, fluid flow inside the fractures is also significant in this case (Figures 5c and 6c) but, as we will demonstrate later, its contribution

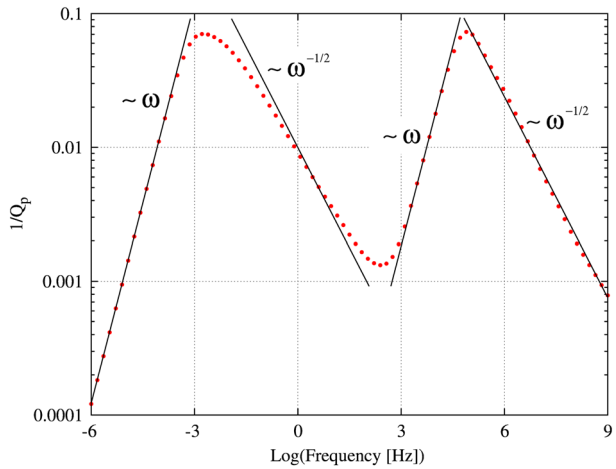

Figure 3. Log-log plot of inverse quality factor as a function of frequency for the sample shown in Figure 1b. The black segments indicate the asymptotic parts of the attenuation curve. Please note that, in order to separate the two attenuation peaks even more, we employ a permeability value of $\kappa^b = 10^{-5}$ mD for the background.

to energy dissipation is negligible. As illustrated by Figure 2, these changes in the WIFF pattern find their corresponding expressions in the observed attenuation and velocity dispersion behavior.

For the frequency at which the second attenuation peak occurs, fluid pressure changes in the background are limited to the immediate vicinity of the fractures (Figures 4b and 4d). This is expected because the corresponding diffusion lengths become smaller as the frequency increases. Accordingly, the effects on attenuation due to FB-WIFF are negligible for this higher frequency. Again, the presence of the quasi-vertical fracture does not change significantly the fluid pressure field when there is no connection between the fractures. In addition, since the diffusion length in the background material is shorter than the distance between the upper tip of the quasi-vertical fracture and the quasi-horizontal fracture, the fluid pressure diffused from the quasi-horizontal fracture into the background does not reach the quasi-vertical fracture. For this reason, fluid flow inside the fractures is largely negligible in this case.

If the fractures intersect, the fluid pressure field changes substantially (compare Figures 4b and 4d). Notably, there is a significant fluid pressure gradient and corresponding fluid flow inside the quasi-vertical

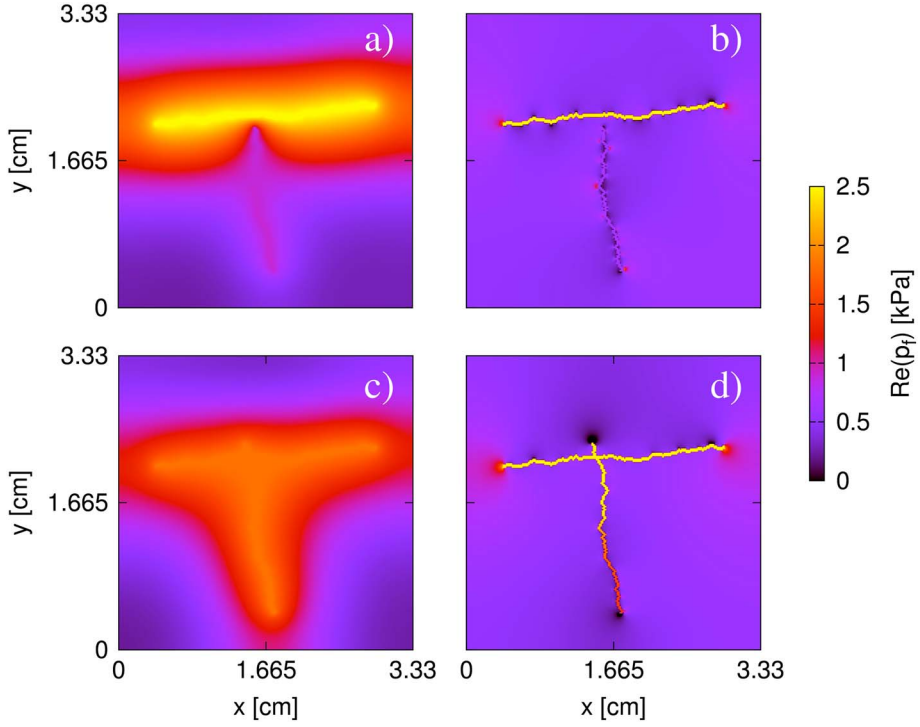

Figure 4. Real part of the fluid pressure. Figures 4a and 4b correspond to the sample shown in Figure 1a, while Figures 4c and 4d correspond to the one shown in Figure 1b. Moreover, Figures 4a and 4c and Figures 4b and 4d denote solutions at frequencies of 1.7 Hz and 82.5 kHz, respectively. The amplitude of the vertical displacement imposed at the top boundary of the sample is 3.33×10^{-9} m; that is, it corresponds to an overall vertical strain amplitude of 10^{-7}.

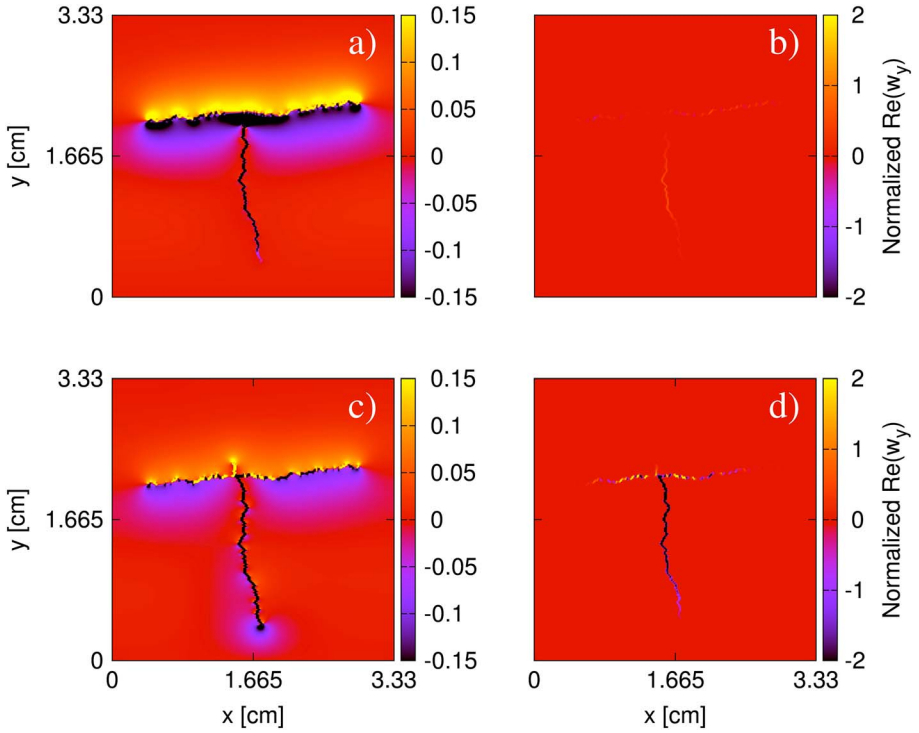

Figure 5. Vertical component of the real part of the relative fluid displacement normalized with respect to the amplitude of the vertical displacement imposed at the top boundary of the sample. Figures 5a and 5b correspond to the sample shown in Figure 1a, while Figures 5c and 5d correspond to the one shown in Figure 1b. Moreover, Figures 5a and 5c and Figures 5b and 5d denote solutions at frequencies of 1.7 Hz and 82.5 kHz, respectively.

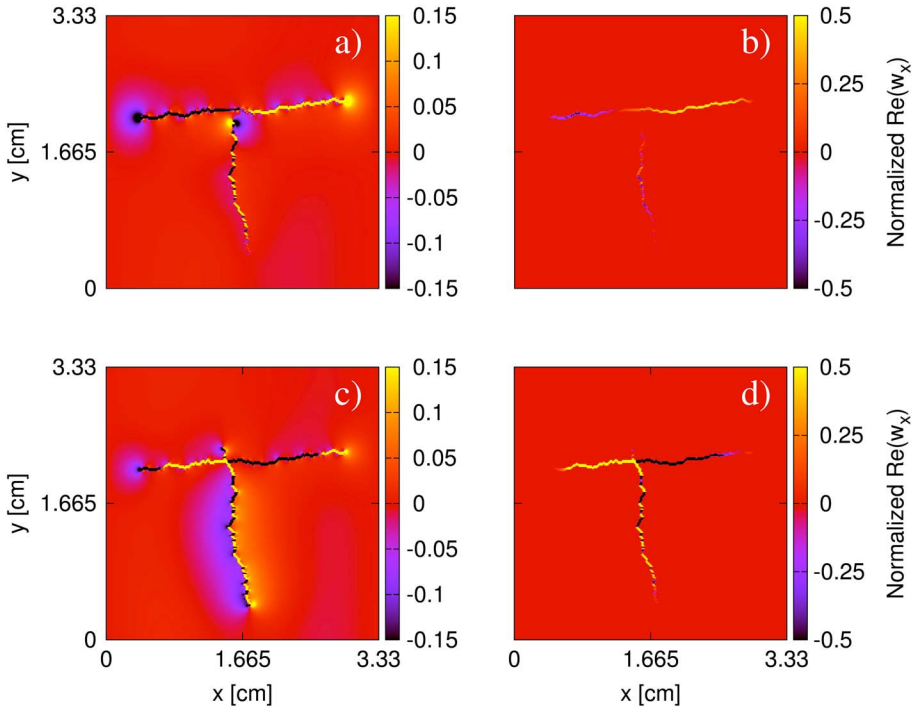

Figure 6. Horizontal component of the real part of the relative fluid displacement normalized with respect to the amplitude of the vertical displacement imposed at the top boundary of the sample. Figures 6a and 6b correspond to the sample shown in Figure 1a, while Figures 6c and 6d correspond to the one shown in Figure 1b. Moreover, Figures 6a and 6c and Figures 6b and 6d denote solutions at frequencies of 1.7 Hz and 82.5 kHz, respectively.

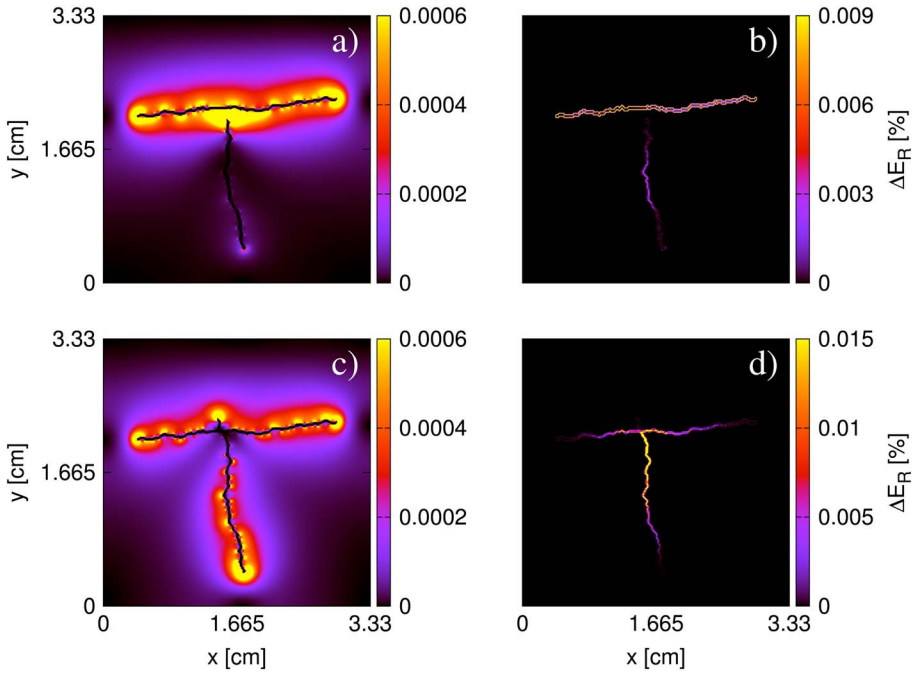

Figure 7. Relative contribution to the total energy dissipation ΔE_R. Figures 7a and 7b correspond to the sample shown in Figure 1a, while Figures 7c and 7d correspond to the one shown in Figure 1b. Moreover, Figures 7a and 7c and Figures 7b and 7d denote solutions at frequencies of 1.7 Hz and 82.5 kHz, respectively.

fracture in the connected situation (Figures 4d and 5d). This fluid is injected from the quasi-horizontal fracture which experiences an increase of fluid pressure in response to the applied strain. Hence, while fluid flow within the quasi-horizontal fracture is not very significant when there is no fracture intersection, it does become substantial when the fractures do intersect. This can be corroborated by comparing Figures 6b and 6d. As illustrated by the blue curve in Figure 2, this enhanced fluid flow arising within the connected fractures generates significant seismic energy dissipation.

3.3. Dissipated Energy Associated With WIFF

Though the relative fluid displacement and pressure fields shown in Figures 4 to 6 give us a qualitative idea of the regions where energy dissipation due to WIFF takes place, they are not the most suitable parameters for a quantitative analysis. Therefore, we directly compute the dissipated energy due to WIFF. If the computational domain is partitioned into a finite number of square grid cells of side length δ, the dissipated power averaged over one wave cycle in a given cell Ω_j is given by [e.g., *Müller and Rothert*, 2006]

$$\Delta E(\Omega_j) = -\frac{1}{2}\mathrm{Re}\left[\dot{\boldsymbol{w}}(\Omega_j)^* \cdot \nabla p_f(\Omega_j)\right]\delta^2, \tag{13}$$

where $\boldsymbol{w}$ is the average relative fluid displacement per unit volume of bulk material and p_f the fluid pressure. Using equation (A2), we get

$$\Delta E(\Omega_j) = \frac{1}{2}\frac{\eta}{\kappa(\Omega_j)}\omega^2\delta^2||\boldsymbol{w}(\Omega_j)||^2\,. \tag{14}$$

This shows that the energy loss is directly proportional to the modulus of relative fluid displacement squared and inversely proportional to the permeability. The total power averaged over one wave cycle dissipated in the rock sample is thus given by

$$\Delta E_T = \sum_{\Omega_j}\frac{1}{2}\frac{\eta}{\kappa(\Omega_j)}\omega^2\delta^2||\boldsymbol{w}(\Omega_j)||^2. \tag{15}$$

Therefore, the relative contribution of a given cell Ω_j to the total energy dissipation can be defined as

$$\Delta E_R(\Omega_j) = \frac{\Delta E(\Omega_j)}{\Delta E_T}100\%. \tag{16}$$

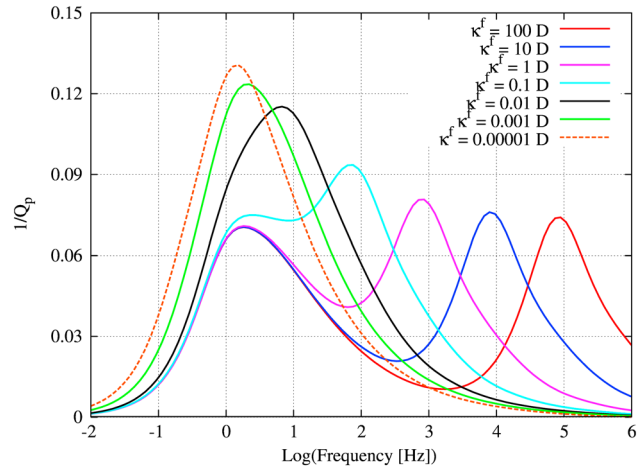

Figure 8. Inverse quality factor for vertically propagating *P* waves as a function of frequency for the sample shown in Figure 1b. The different colors indicate the responses obtained for different values of fracture permeability, as denoted in the legend.

This is a suitable parameter to quantitatively analyze the contribution of the different regions of the considered samples to attenuation due to WIFF.

Figure 7 shows the spatial distribution of ΔE_R for the samples and frequencies considered before. That is, Figures 7a and 7b correspond to the sample shown in Figure 1a and Figures 7c and 7d to the sample shown in Figure 1b. In addition, Figures 7a, 7c and 7b, 7d depict the responses for frequencies of 1.7 Hz and 82.5 kHz, respectively. We observe that in the unconnected scenario (Figures 7a and 7b), most of the energy dissipation takes place in the background material surrounding the quasi-horizontal fracture due to FB-WIFF. That is, even though fluid flow inside the fractures can be significant in these cases (see Figures 5a, 5b, 6a, and 6b), the corresponding contribution to total attenuation is rather negligible. This is because the fluid displacement in these regions is comparable to that of the background fluid in the vicinity of the quasi-horizontal fracture. Therefore, since the energy dissipation is inversely proportional to permeability (equation (14)), the relative contribution of the highly permeable fractures fluid ends up being negligible compared to that occurring in the weakly permeable background. It can also be seen that for the frequency of the second attenuation peak the energy dissipation occurs in the immediate vicinity of the quasi-horizontal fracture, as expected. In order to quantify the total relative contribution of fluid flow within the fractures to attenuation, we summed up the local contributions of the cells composing the fractures. It turned out to be 0.0002% for the frequency of the first attenuation peak and 9% for that of the second peak. Taking into account that attenuation levels are negligible for the situation depicted by Figure 7b, we can conclude that the contribution of FF-WIFF to energy dissipation is negligible in the absence of connectivity.

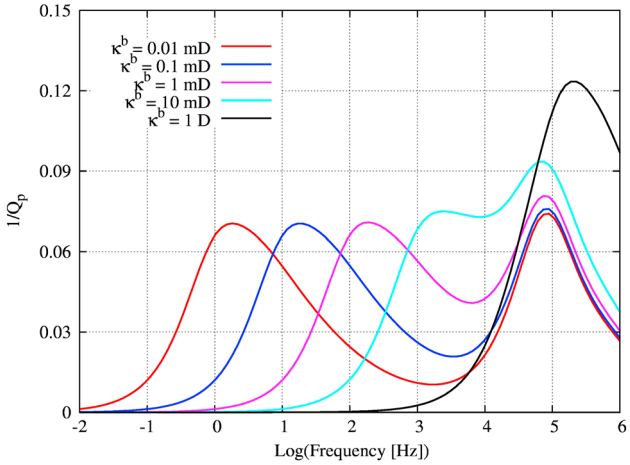

Figure 9. Inverse quality factor for vertically propagating *P* waves as a function of frequency for the sample shown in Figure 1b. The different colors indicate the responses obtained for different values of the permeability of the background material, as denoted in the legend.

For the connected scenario, the situation is different. For the frequency of the first attenuation peak (Figure 7c), the total relative contribution of fluid flow within the fractures also turned out to be negligible (~ 0.005%). In this case, most of the energy is dissipated in the background material due to FB-WIFF. Indeed, Figure 7c allows to see more clearly that, apart from the energy losses arising in the vicinity of the quasi-horizontal fracture, a significant part of energy dissipation takes place in the vicinity of the quasi-vertical fracture (compare Figures 7a and 7c). For the frequency of the second attenuation peak, we observe that very significant levels of energy dissipation take place within both fractures (Figure 7d).

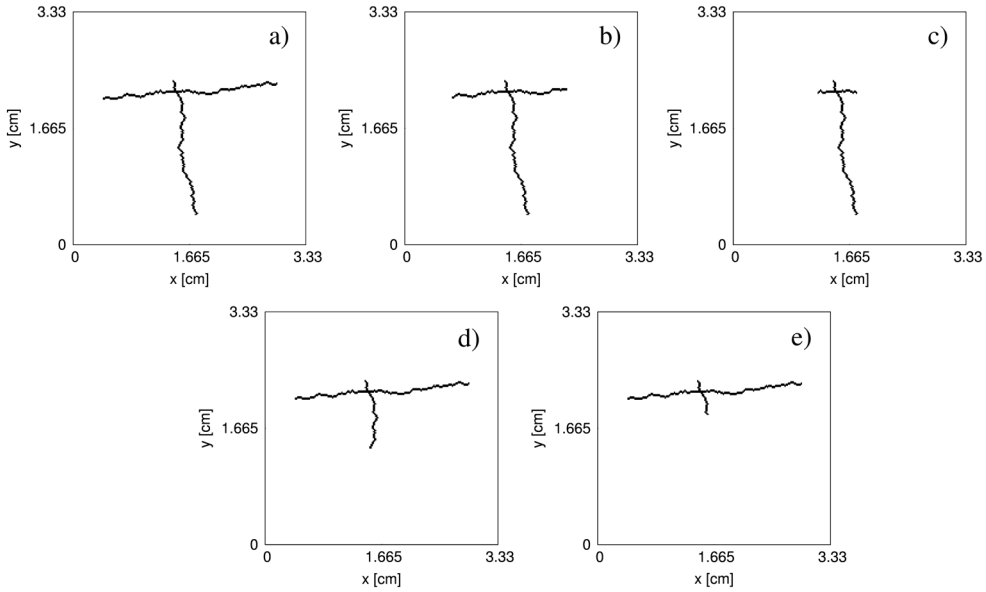

Figure 10. Synthetic rock samples designed to analyze the sensitivity of attenuation due to WIFF in relation to the lengths of connected fractures.

In this case, the total relative contribution of FF-WIFF to attenuation turned out to be 98.23%, thus illustrating the importance of this energy loss mechanism.

These results therefore indicate that, while the contribution to seismic attenuation due to FF-WIFF is negligible in the absence of fracture connectivity, it can be very important whenever fractures do intersect. Indeed, for the parameters considered in this analysis, energy dissipation at the frequency of the second attenuation peak predominantly occurs due to FF-WIFF.

3.4. Characteristics of Attenuation Due to FF-WIFF

3.4.1. Sensitivity to the Permeabilities of the Fracture and the Background Materials

According to equation (8), the transition frequency ω_c^f of the FF-WIFF attenuation peak is directly proportional to the pressure diffusivity of the fracture material and, therefore, to its permeability. In order to verify this dependence, we show in Figure 8 the inverse quality factor for the sample of Figure 1b for different values of fracture permeability. We see that the transition frequency of the first attenuation peak ω_c^b is not sensitive to the fracture permeability and remains unchanged at a value of $\sim$ 1.7 Hz. Conversely, and in agreement with equation (8), the second attenuation peak shifts toward higher frequencies with increasing κ^f for values above $\sim$ 10 mD. For κ^f values below $\sim$ 1 mD, the attenuation is, however, not very sensitive to the fracture permeability and the aforementioned relation between ω_c^f and κ^f is not valid. This is expected as when the background permeability is comparable to that of the fracture material, the fluid will have enough time to flow into the background during each oscillatory half-cycle, and hence, the simple relation between ω_c^f and κ^f depicted by equation (8) does not hold any longer. Moreover, it is interesting to notice that in these cases, the two attenuation peaks collapse into one very prominent single peak corresponding to very low Q_p values. By comparing such attenuation

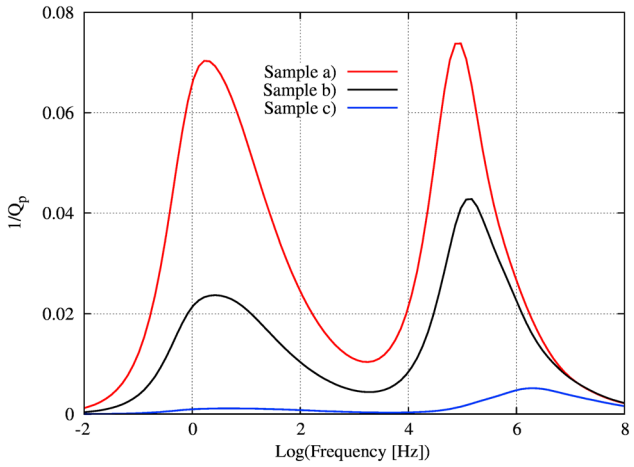

Figure 11. Inverse quality factor for vertically propagating *P* waves as a function of frequency for the samples shown in Figures 10a–10c.

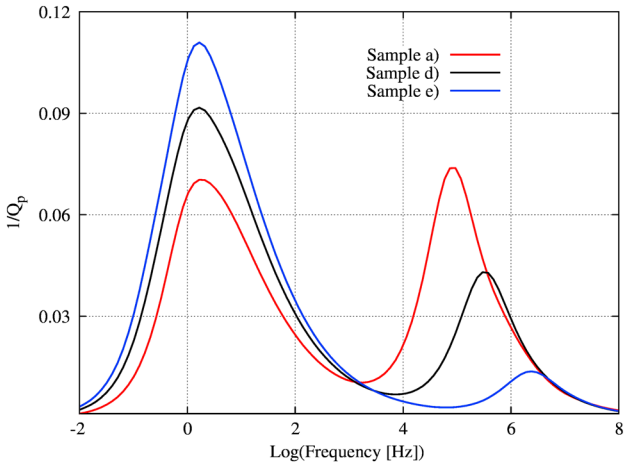

Figure 12. Inverse quality factor for vertically propagating *P* waves as a function of frequency for the samples shown in Figures 10a, 10d, and 10e.

curves with those of Figure 2, we can verify that when κ^f and κ^b are comparable, this single attenuation peak is very similar to that corresponding to the unconnected scenario. This, in turn, illustrates that when the permeability of the fracture material is comparable or smaller than that of the background, the fractures do no longer constitute preferential fluid pathways. Correspondingly, the fluid is not channelized into the quasi-vertical fracture as result of the applied strain. This makes the relative contribution of FF-WIFF negligible, and hence, seismic attenuation is mainly controlled by FB-WIFF.

To study the role played by the permeability of the embedding matrix, we perform a corresponding analysis by varying the permeability of the background material. Figure 9 shows the inverse quality factor corresponding to the sample of Figure 1b for different values of background permeability. We observe that while, in agreement with equation (7), the transition frequency corresponding to FB-WIFF shifts toward higher frequencies as the permeability increases, the second attenuation peak remains unaffected. Moreover, for a background permeability of 1 D, the permeability of the background and that of the fracture are comparable, and correspondingly, seismic attenuation is mainly controlled by FB-WIFF. For this reason, the two attenuation peaks collapse into a single prominent peak with very low Q_p values.

3.4.2. Sensitivity to the Lengths of the Fractures

To study the dependence between the characteristics of the attenuation peak related to FF-WIFF and the lengths of the fractures, we first focus on the role played by the length of the quasi-horizontal fracture. We consider three different values for this parameter while keeping the quasi-vertical fracture unchanged (Figures 10a–10c). Figure 11 shows the inverse quality factor as a function of frequency for the three

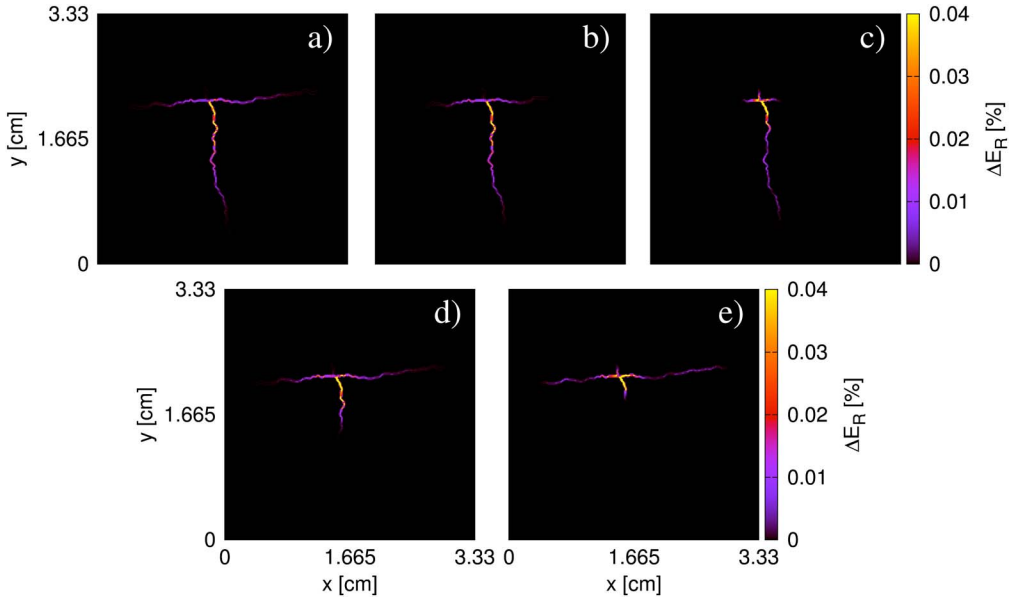

Figure 13. Relative local contribution to the total energy dissipation ΔE_R for the samples shown in Figure 10. In each case, these fields were computed at the frequencies of the corresponding FF-WIFF attenuation peaks shown in Figures 11 and 12.

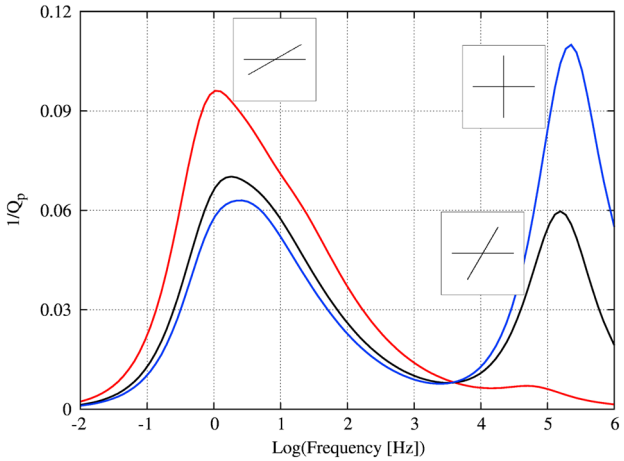

Figure 14. Inverse quality factor for vertically propagating *P* waves as a function of frequency for samples containing two fractures of equal length intersecting at their centers at angles of 30°, 60°, and 90°.

samples. We see that the magnitude of the FF-WIFF attenuation diminishes as the length of the quasi-horizontal fracture decreases. This is expected, since the fluid pressure increase in the quasi-horizontal fracture as result of the applied strain becomes less significant as the fracture length is reduced. Consequently, the induced fluid pressure gradient in the quasi-vertical fracture is also less significant, thus resulting in less fluid flow and seismic attenuation. Correspondingly, the amplitude of the FB-WIFF attenuation peak also diminishes as the length of the quasi-horizontal fracture decreases. In this context, it is also interesting to note that the transition frequency ω_c^f shifts toward higher frequencies as the length of the quasi-horizontal fractures decreases.

In order to explore the role played by the length of the quasi-vertical fracture, we include in Figure 12 the inverse quality factor as a function of frequency for the samples shown in Figures 10a, 10d, and 10e. The corresponding results indicate that FF-WIFF attenuation levels become less significant and that the attenuation peak shifts toward higher frequencies as the length of the quasi-vertical fracture is reduced. Moreover, the amplitude of the FB-WIFF attenuation peak increases as the length of the quasi-vertical fracture is

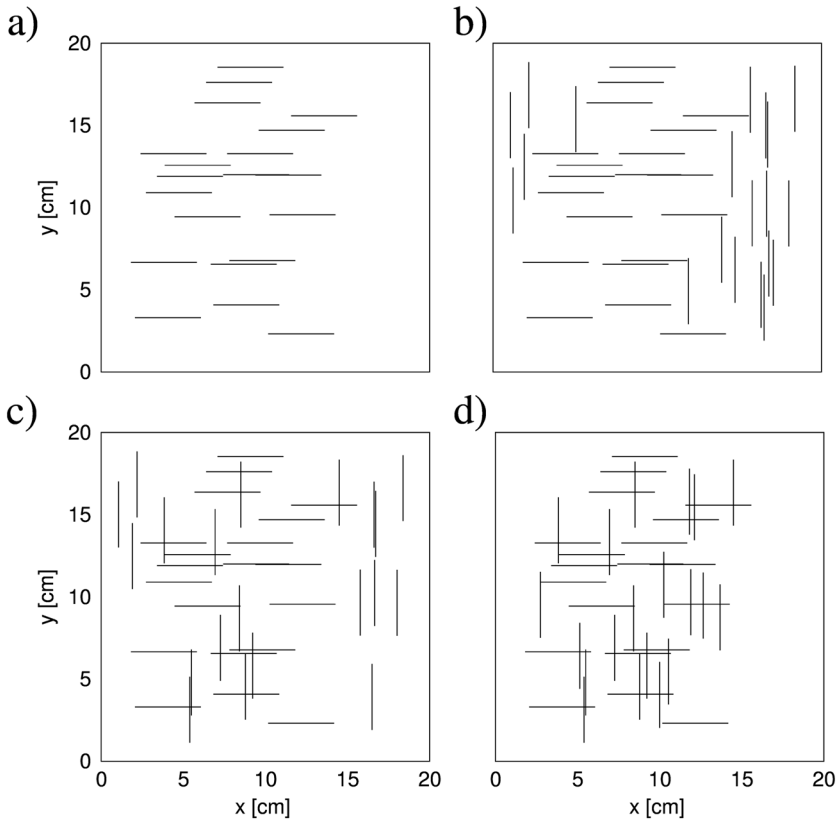

Figure 15. Synthetic rock samples designed to analyze the role played by the degree of connectivity of fracture networks on seismic attenuation due to WIFF.

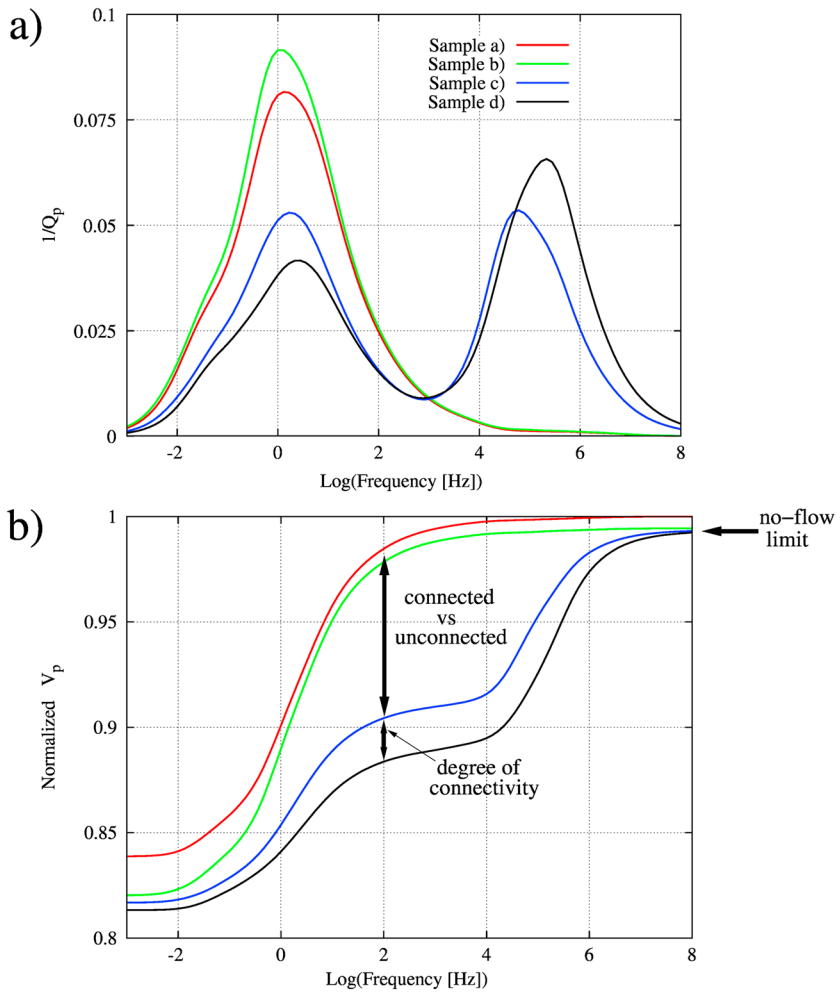

Figure 16. (a) Inverse quality factor and (b) phase velocity normalized with respect to the no-flow limit velocity of the sample shown in Figure 15a for vertically propagating *P* waves as functions of frequency for the samples shown in Figure 15.

reduced. An important result emerging from this analysis is that the lengths of both the quasi-vertical and quasi-horizontal fractures are involved in the definition of the characteristic length a_f of the fractures.

To better understand the results depicted in Figures 11 and 12, we show in Figure 13 the relative local contribution to the total energy dissipation for the samples depicted in Figure 10. In each case, we evaluate these fields at the frequencies of the corresponding FF-WIFF attenuation peaks. We see that, although the most important part of energy dissipation seems to occur in the lower segment of the quasi-vertical fracture, significant energy losses also occur in the quasi-horizontal fracture. This in turn indicates that the fracture network has to be considered as an entity and that the various subsegments composing the fractures are involved in the definition of the characteristic length scale a_f. It is interesting to note that most of the energy dissipation shown in Figure 13 is due to FF-WIFF. Indeed, the total relative contribution of flow within the fractures to attenuation turned out to be above 98% in all considered cases, thus illustrating the importance of this energy loss mechanism.

3.4.3. Sensitivity to the Intersection Angle of the Fractures

In order to analyze the role of the intersection angle between two fractures on attenuation, we evaluate the inverse quality factor as a function of frequency for a sample containing two fractures of equal length intersecting at their centers. One of the fractures is located horizontally aligned in the center of a square rock sample of side length 3.33 cm and intersected by the other one at an angle θ of 30°, 60°, and 90°. The corresponding results are shown in Figure 14. We observe that while this parameter does not change significantly the location of the two attenuation peaks, it strongly influences their magnitudes. In fact, we see that

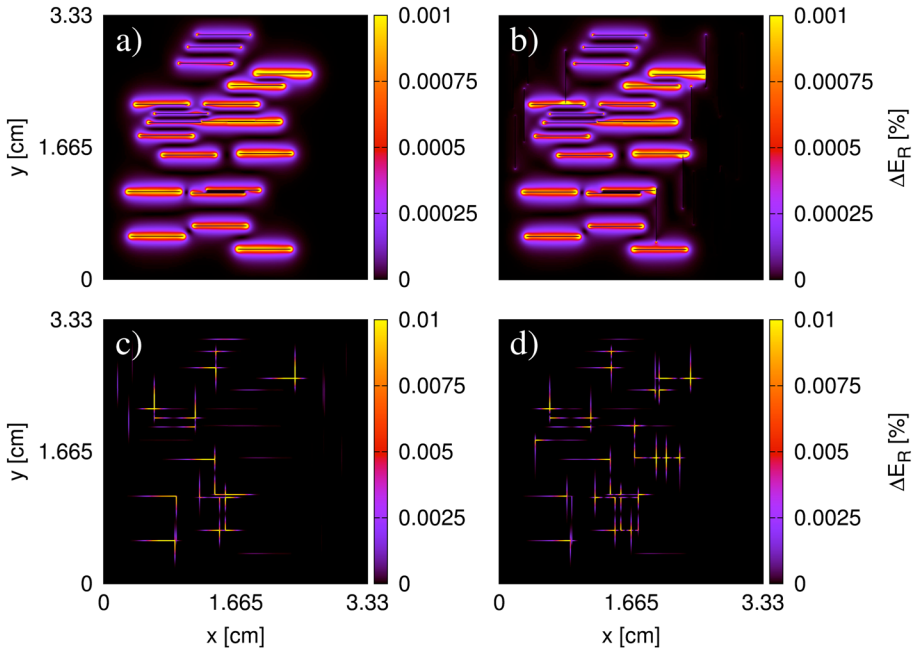

Figure 17. Relative local contribution to the total energy dissipation ΔE_R for the samples shown in Figure 15. These fields were computed at the frequencies of the corresponding attenuation peaks related to (a and b) FB-WIFF and (c and d) FF-WIFF.

the attenuation peak related to FF-WIFF is highest for $\theta = 90°$ and gets smaller as θ decreases. Conversely, the magnitude of the peak produced by FB-WIFF is lowest for $\theta = 90°$ and increases as θ decreases. This is expected, because as the nonhorizontal fracture gets more horizontal the strain applied on the rock sample starts to increase its fluid pressure, and thus, the amount of fluid injected from the horizontal fracture gets less significant. This in turn causes the fluid pressure gradient between the fractures and the background to increase, whereas the amount of fluid flow within the fractures becomes less significant. Hence, the levels of attenuation related to the first peak increase while the magnitude of the second peak decreases as the nonhorizontal fracture approaches a horizontal position.

4. Seismic Signatures of Fracture Network Connectivity

The degree of connectivity of fracture networks is a key parameter that controls the prevailing effective hydraulic properties of fractured media. In order to identify the corresponding information that may be encoded in seismic data, we consider the four samples shown in Figure 15. The sample shown in Figure 15a contains 20 horizontal fractures, while in the one depicted in Figure 15b we add 20 vertical fractures that are not connected to the horizontal ones. Samples in Figures 15c and 15d both contain 20 horizontal and 20 vertical fractures but differ in terms of their interconnectivity. In the sample shown in Figure 15c, 10 pairs of fractures are connected, whereas in the one depicted in Figure 15d, most fractures are connected. In all cases, the sample is a square of side length 20 cm, and the lengths and apertures of the fractures are 4 cm and 0.06 cm, respectively. The properties of the background material are similar to those used in the previous experiments, while the elastic properties of the dry frame of the fracture material were computed according to equations (11) and (12).

Figure 16a depicts the inverse quality factor of the samples shown in Figure 15 as a function of frequency for vertically incident *P* waves. As expected based on our previous observations, we see in Figure 16a that the samples shown in Figures 15a and 15b exhibit a single clear attenuation peak with high levels of energy dissipation related to FB-WIFF, whereas the ones depicted in Figures 15c and 15d also have a second attenuation peak due to FF-WIFF. For the samples shown in Figures 15c and 15d, the amplitude of the first peak diminishes as compared with the responses for the samples shown in Figures 15a and 15b. This reduction in FB-WIFF energy dissipation is more significant for the sample shown in Figure 15d, which is characterized

by a higher degree of fracture connectivity, and is associated with a more significant attenuation due to FF-WIFF. We also observe that the second attenuation peak moves toward higher frequencies with increasing degree of fracture connectivity.

Figure 16b shows that the phase velocity also contains valuable information with regard to the degree of fracture connectivity. We observe that velocity dispersion effects occur over a wider frequency range in the presence of fracture connectivity and that the particular characteristics of the changes of phase velocity with frequency depend on the degree of connectivity. Correspondingly, measurable differences in phase velocity for seismic frequencies may prevail depending on the degree of fracture connectivity. For the particular physical parameters and geometries employed in the analysis, significant discrepancies between the phase velocities corresponding to the different scenarios take place at a frequency of $\sim$ 100 Hz. Indeed, we observe in Figure 16b a phase velocity decrease of $\sim$ 8% between the unconnected scenarios of the samples shown in Figures 15a and 15b and the mildly connected situation represented by the sample in Figure 15c. A further significant velocity reduction is associated with the increase in fracture connectivity of the sample shown in Figure 15d as compared to the sample depicted in Figure 15c.

In order to explore these WIFF effects in more detail, we show in Figure 17 the relative local contribution to the total energy dissipation for the considered samples. In Figures 17a and 17b, we computed ΔE_R at the frequencies of the corresponding FB-WIFF attenuation peaks, whereas in Figures 17c and 17d, the locations of the peaks related to FF-WIFF were considered. We observe that the energy dissipation fields shown in Figures 17a and 17b are quite similar, which demonstrates that the presence of the vertical unconnected fractures does not affect significantly the prevailing WIFF patterns. Moreover, we see that in these cases, the energy dissipation takes place mainly in the background in the vicinity of the horizontal fractures. Indeed, the total relative contribution of fluid flow within the fractures to attenuation turns out to be negligible ($<$ 0.001%). Conversely, energy dissipation in Figures 17c and 17d takes place within the connected fractures and is confined to the vicinity of the fracture intersections. Indeed, the total relative contribution of FF-WIFF to attenuation exceeds 99% in these cases. As expected, the region where WIFF is significant seems to be larger for the sample shown in Figure 15d, for which the degree of fracture connectivity is higher. Since for this sample the attenuation peak is located at higher frequencies compared to the sample shown in Figure 17c, the characteristic length at which fluid flow is significant is smaller.

5. Discussion

A conceptual simplification used in this study is that the results are based on numerical simulations performed on two-dimensional samples, which implies that the fractures extend infinitely in the out-of-plane axis. Although this is formally incorrect, the quasi-planar nature of many fractures partially justifies this assumption and hence allows for valuable insights into the first-order WIFF effects expected to prevail in real fracture systems.

Conventionally, a single fracture is conceptualized as a pair of parallel interfaces separated by a constant distance referred to as aperture. This simple model is valid only for smooth fracture surfaces and sufficiently low normal stress with regard to the fracture plane [*Liu*, 2005]. Natural fractures tend to be "rough-walled," with the walls being in contact with each other at certain locations. Both the number and the spatial extension of these contact areas are expected to increase with increasing normal stress. Given that these characteristics of fractures control their mechanical and hydraulic properties [e.g., *Pyrak-Nolte and Morris*, 2000], it is expected that the two manifestations of WIFF observed in fractured media are highly sensitive to the effective pressure conditions of the probed medium. Moreover, the regions between the contact areas often contain rock fragments, weathering products, or mineral deposits, which further enhance the tortuosity of the fluid pathways across the fracture. In view of all this, it is reasonable to represent fractures as parts of the poroelastic continuum. Indeed, this conceptualization is consistent with the models proposed by *Liu et al.* [2000] for describing the effective elastic properties of fractured rocks and is commonly employed to simulate groundwater flow in fractured media [e.g., *Liu and Bodvarsson*, 2001; *Guarracino and Quintana*, 2009].

The results presented in this work are valid for mesoscopic fractures; that is, the relevant length scales associated with the fractures must obey equation (1). In addition, we assumed quasi-static poroelastic behavior

to infer the seismic attenuation and velocity dispersion signatures, which in turn implies that the frequency is smaller than the characteristic Biot frequency [e.g., *Biot*, 1962; *Dutta and Odé*, 1979]

$$\omega_B = \frac{\phi\eta}{\kappa\rho_f}. \tag{17}$$

It also means that the FF-WIFF characteristic frequency (equation (8)) should be smaller than ω_B. However, simple inspection for the used fracture parameters yields $f_B = \omega_B/2\pi \approx 0.75$ kHz, therefore suggesting that, at least in some of the situations considered in this work, the FF-WIFF attenuation peak is outside the validity range of the quasi-static poroelastic equations. Nevertheless, we believe that the corresponding results are physically meaningful, because seismic attenuation also occurs if $\omega \geq \omega_B$. In this high-frequency regime, energy dissipation takes place in the viscous boundary layers; that is, it does not result from wave-induced pressure diffusion but from vorticity diffusion [*Müller and Sahay*, 2011]. There is evidence to suggest that the transition from pressure to vorticity diffusion around $\omega \approx \omega_B$ is gradual and smooth, which in turn implies that the energy dissipation estimates based on quasi-static poroelastic simulations are approximately correct even if $\omega \geq \omega_B$. In this context, it is also important to remark that the present analysis indicates that, even if the attenuation peak related to FF-WIFF is located outside the seismic frequency band, the presence of connected fractures also affects the characteristics of the attenuation peak due to FB-WIFF in a significant manner. This, in turn, indicates that even in the unfavorable case in which the attenuation peak produced by FF-WIFF is not visible in the seismic frequency band, seismic data may contain valuable information on fracture connectivity.

Another interesting point is that the FF-WIFF arising in the presence of fracture connectivity can be regarded as the mesoscopic analog of the squirt flow mechanism identified by *Mavko and Nur* [1975]. The latter prevails at microscopic scales and requires that two or more grain-scale cracks of different orientation are hydraulically connected. Consequently, stress changes cause fluid flow from one crack into another and thus energy dissipation. It is worth noting that, although the methodology outlined in this study accounts for the presence of mesoscopic fractures only, it is straightforward to accommodate the combined effects of WIFF due to both microscopic and mesoscopic fractures by following a procedure similar to that proposed by *Rubino and Holliger* [2013].

For the sake of simplicity, the analysis performed in this work only focuses on the additional manifestation of WIFF that arises when a compressional wave propagates through a rock containing connected fractures. It is, however, expected that a similar manifestation of WIFF exists for shear waves. Analyzing the effects of fracture connectivity on the attenuation and dispersion of shear waves is of relevance, since shear and compressional waves may be used in complementary ways for characterizing fractured media. The corresponding analysis can be performed by applying numerical shear experiments on rock samples containing connected and unconnected fractures, which will be the subject of forthcoming studies.

In this paper we only analyzed the seismic signatures of vertically propagating *P* waves. Aligned mesoscopic fractures result in an overall transversally isotropic (TI) effective medium, while two intersecting fracture sets can result in monoclonic symmetry [*Tsvankin*, 2012]. *Chapman* [2009] studied the frequency-dependent anisotropy of a rock mass permeated by two sets of aligned mesoscopic fractures. The frequency dependence arises because there is a wave-induced fluid pressure equilibration between the fractures and the surrounding equant pores. The resulting seismic attenuation and velocity dispersion characteristics are due to FB-WIFF only, while the contribution of FF-WIFF is not contained in this model. Our results do, however, suggest that FF-WIFF is an important feature of seismic attenuation and velocity dispersion in fractured rocks, and correspondingly, ignoring its effects can produce significant errors with regard to the seismic characterization of these kinds of materials. Future work should therefore analyze the combined effects of anisotropy as well as FB-WIFF and FF-WIFF on seismic wave propagation in fractured media.

6. Conclusions

We have used numerical oscillatory relaxation simulations based on the quasi-static poroelastic equations to study the role played by fracture connectivity on the characteristics of WIFF between fractures and the embedding matrix as well as within connected fractures. We verified that, in the absence of fracture connectivity, mesoscopic fractures oriented perpendicularly to the direction of wave propagation generate strong *P* wave attenuation and velocity dispersion due to WIFF between the fractures and the embedding

porous matrix. However, as soon as such fractures are intersected by others, the seismic signatures change rather dramatically. In particular, a decrease in the attenuation peak related to the unconnected scenario together with the appearance of a second attenuation peak associated with high levels of attenuation can be observed. These effects become stronger as the connectivity degree of the fracture network increases. In addition, velocity dispersion in the presence of connected fractures prevails within a broader frequency range, thus producing a noticeable velocity reduction for certain frequencies compared to the unconnected scenario. We have computed the spatial distributions of the induced fluid pressure, relative fluid displacement, and the local energy dissipation to explore the physical processes involved in the different scenarios. This allowed us to confirm that the additional manifestation of WIFF arising in the presence of fracture connectivity is indeed produced by fluid flow within fractures.

We have also performed an exhaustive analysis to study the role played by different characteristics of the fracture network on the two manifestations of WIFF arising in the presence of fracture connectivity. We observed that in these cases, seismic attenuation and phase velocity are sensitive to key characteristics of the fractured medium, namely to the permeabilities, lengths, and intersection angles of the fractures as well as to the degree of connectivity of the fracture network.

Since fractured rock masses typically show a certain degree of connectivity, the corresponding additional WIFF manifestation must be accounted for in order to model realistic seismic wave propagation in these kinds of environments. Moreover, given that these effects contain critical information regarding the hydraulic properties of fractured rocks, we believe that additional research on this topic, both computational and laboratory-based, may eventually open avenues for extracting this type of information from seismic data.

Appendix A: Numerical Analysis of Quasi-Static Poroelasticity

Numerical analysis of seismic attenuation and velocity dispersion due to WIFF in the presence of mesoscopic fractures is challenging. This is mainly due to the fact that, in the low-frequency range, the spatial scales at which pressure diffusion occurs are very small compared with the seismic wavelengths. This is compounded by the necessity to employ small enough grid spacings to properly discretize the fractures, which is an issue both in the low- and high-frequency ranges. To overcome these problems, we employ a numerical upscaling procedure similar to that presented by *Rubino et al.* [2009]. We do, however, impose strain boundary conditions instead of stress boundary conditions, as relaxation experiments turned out to be more suitable for analyzing the *P* wave seismic response of rock samples containing very strong compressibility contrasts (M. Milani, personal communication, 2014). In addition, as suggested by *Wenzlau et al.* [2010] and *Quintal et al.* [2011], we solve *Biot* [1941] quasi-static consolidation equations rather than *Biot* [1962] equations of dynamic poroelasticity. The reasoning behind this is that, since WIFF is controlled by fluid pressure diffusion, we can neglect the inertial forces, which in turn provides us with a more efficient procedure to estimate the corresponding effects.

The equations of quasi-static poroelasticity [*Biot*, 1941] in the space-frequency domain are

$$\nabla \cdot \boldsymbol{\sigma} = \mathbf{0}, \tag{A1}$$

$$i\omega \frac{\eta}{\kappa} \boldsymbol{w} = -\nabla p_f, \tag{A2}$$

where $\boldsymbol{\sigma} \equiv (\sigma_{ij})$ is the total stress tensor, $\boldsymbol{w}$ the average relative fluid displacement per unit volume of bulk material, and p_f the fluid pressure. Equations (A1) and (A2) represent the stress equilibrium within the sample and Darcy's law, respectively. These two expressions are coupled through the stress-strain relations

$$\sigma_{ij} = 2\mu_m \epsilon_{ij}(\boldsymbol{u}^s) + \delta_{ij}\left(\lambda_u \nabla \cdot \boldsymbol{u}^s - \alpha M \zeta\right), \tag{A3}$$

$$p_f = -\alpha M \nabla \cdot \boldsymbol{u}^s + M\zeta, \tag{A4}$$

where $\boldsymbol{u}^s$ is the average displacement vector of the solid phase, $\epsilon_{ij}(\boldsymbol{u}^s) = \frac{1}{2}\left(\partial u_i^s/\partial x_j + \partial u_j^s/\partial x_i\right)$ denotes the strain tensor of the solid phase, $\zeta = -\nabla \cdot \boldsymbol{w}$ represents the change in fluid content, and λ_u is the saturated Lamé parameter, which is given by

$$\lambda_u = K_m + \alpha^2 M - \frac{2}{3}\mu_m. \tag{A5}$$

To compute WIFF effects, equations (A1) through (A4) are solved under proper boundary conditions. That is, a time-harmonic vertical solid displacement of the form $\Delta u\, e^{i\omega t}$ is applied at the top boundary of a two-dimensional rectangular poroelastic medium containing mesoscopic fractures, which produces a time-harmonic overall vertical strain of amplitude $\epsilon_v = \Delta u/L$, where L is the vertical side length of the sample. No tangential forces are imposed on the boundaries of the sample and the solid is neither allowed to move on the bottom boundary nor to have horizontal displacements on the lateral boundaries. The fluid is neither allowed to flow into the sample nor out of it. In order to estimate the stress and strain fields, equations (A1) through (A4) are solved using a finite element procedure. We use bilinear functions to approximate the solid displacement vector and a closed subspace of the vector part of the Raviart-Thomas-Nedelec space of zero order for the fluid displacement. Under the assumption that the heterogeneous rock sample can be represented by an equivalent homogeneous viscoelastic solid, it is possible to calculate an equivalent undrained complex plane-wave modulus corresponding to the vertical direction of wave propagation, $\overline{M_c}(\omega)$, by using the relation

$$\overline{M_c}(\omega) = \frac{\overline{\sigma}(\omega)}{\epsilon_v}, \tag{A6}$$

where $\overline{\sigma}(\omega)$ denotes the vertical component of the stress field averaged over the sample's volume. Then, the corresponding complex compressional velocity is given by

$$V_{pc}(\omega) = \sqrt{\frac{\overline{M_c}(\omega)}{\overline{\rho_b}}}, \tag{A7}$$

where $\overline{\rho_b}$ is the average bulk density of the numerical rock sample, that is,

$$\overline{\rho_b} = \frac{1}{V}\int_\Omega \left(\phi\rho_f + (1-\phi)\rho_s\right) \mathrm{d}V, \tag{A8}$$

with ρ_s and ρ_f being the density of solid grains and pore fluid, respectively. Finally, the equivalent compressional phase velocity $V_p(\omega)$ and inverse quality factor $Q_p(\omega)$ are [*Rubino et al.*, 2009]

$$V_p(\omega) = \left[\mathrm{Re}\left(\frac{1}{V_{pc}(\omega)}\right)\right]^{-1}, \tag{A9}$$

$$\frac{1}{Q_p(\omega)} = \frac{\mathrm{Im}(V_{pc}(\omega)^2)}{\mathrm{Re}(V_{pc}(\omega)^2)}. \tag{A10}$$

This numerical algorithm does not only allow for computing seismic attenuation and phase velocity but also for obtaining the spatial distributions of the main poroelastic parameters, such as the induced fluid pressure and the relative fluid displacement. These fields are very useful for identifying and exploring the governing physical mechanisms producing seismic attenuation in fractured media.

Acknowledgments

This work was supported in part by grants from the Swiss National Science Foundation, the Agencia Nacional de Promoción Científica y Tecnológica (PICT 2010-2129), Argentina, and the Herbette Foundation of the University of Lausanne. The authors thank Marina Rosas Carbajal for her help to improve the algorithm for the oscillatory relaxation tests. Constructive comments by the Associate Editor, Douglas Schmitt, and an anonymous reviewer greatly helped to improve the quality of this manuscript. The data derived by the numerical simulations and the underlying models can be obtained free of charge upon request from the lead-author.

References

Bakulin, A., V. Grechka, and I. Tsvankin (2000), Estimation of fracture parameters from reflection seismic data - Part I: HTI model due to a single fracture set, *Geophysics*, *65*, 1788–1802.

Berkowitz, B., O. Bour, P. Davy, and N. Odling (2000), Scaling of fracture connectivity in geological formations, *Geophys. Res. Lett.*, *27*, 2061–2064.

Biot, M. A. (1941), General theory of three-dimensional consolidation, *J. Appl. Phys.*, *12*, 155–164.

Biot, M. A. (1962), Mechanics of deformation and acoustic propagation in porous media, *J. Appl. Phys.*, *33*, 1482–1498.

Brajanovski, M., B. Gurevich, and M. Schoenberg (2005), A model for *P* wave attenuation and dispersion in a porous medium permeated by aligned fractures, *Geophys. J. Int.*, *163*, 372–384.

Chapman, M. (2003), Frequency-dependent anisotropy due to meso-scale fractures in the presence of equant porosity, *Geophys. Prospect.*, *51*, 369–379.

Chapman, M. (2009), Modeling the effect of multiple sets of mesoscale fractures in porous rocks on frequency-dependent anisotropy, *Geophysics*, *74*, D97–D103.
Clark, R. A., P. M. Benson, A. J. Carter, and C. A. Guerrero Moreno (2009), Anisotropic *P* wave attenuation measured from a multi-azimuth surface seismic reflection survey, *Geophys. Prospect.*, *57*, 835–845.
Dutta, N. C., and H. Odé (1979), Attenuation and dispersion of compressional waves in fluid-filled porous rocks with partial gas saturation (White model)—Part I: Biot theory, *Geophysics*, *44*(11), 1777–1788.
Guarracino, L., and F. Quintana (2009), A constitutive model for water flow in unsaturated fractured rocks, *Hydrol. Process.*, *23*, 697–701.
Gurevich, B., M. Brajanovski, R. J. Galvin, T. M. Müller, and J. Toms-Stewart (2009), P-wave dispersion and attenuation in fractured and porous reservoirs—Poroelasticity approach, *Geophys. Prospect.*, *57*, 225–237.
Hardebeck, J. L., and E. Hauksson (1999), Role of fluids in faulting inferred from stress field signatures, *Science*, *285*, 236–239.
Kilburn, C. R. J. (2003), Multiscale fracturing as a key to forecasting volcanic eruptions, *J. Volcanol. Geoth. Res.*, *125*, 271–289.
Krief, M., J. Garat, J. Stellingwerff, and J. Ventre (1990), A petrophysical interpretation using the velocities of *P* and *S* waves (full waveform inversion), *The Log Analyst*, *31*, 355–369.
Legarth, B., E. Huenges, and G. Zimmermann (2005), Hydraulic fracturing in a sedimentary geothermal reservoir: Results and implications, *Int. J. Rock Mech. Min. Sc.*, *42*, 1028–1041.
Liu, E. (2005), Effects of fracture aperture and roughness on hydraulic and mechanical properties of rocks: Implication of seismic characterization of fractured reservoirs, *J. Geophys. Eng.*, *2*, 38–47.
Liu, E., J. A. Hudson, and T. Pointer (2000), Equivalent medium representation of fractured rock, *J. Geophys. Res.*, *105*, 2981–3000.
Liu, E., M. Chapman, I. Varela, X. Li, J. H. Queen, and H. Lynn (2007), Velocity and attenuation anisotropy: Implication of seismic fracture characterizations, *The Leading Edge*, *26*, 1170–1174.
Liu, H. H., and G. S. Bodvarsson (2001), Constitutive relations for unsaturated flow in a fracture network, *J. Hydrol.*, *252*, 116–125.
Maultzsch, S., M. Chapman, E. Liu, and X. Y. Li (2003), Modelling frequency-dependent seismic anisotropy in fluid-saturated rock with aligned fractures: Implication of fracture size estimation from anisotropic measurements, *Geophys. Prospect.*, *51*, 381–392.
Mavko, G., and A. Nur (1975), Melt squirt in the asthenosphere, *J. Geophys. Res.*, *80*, 1444–1448.
Mavko, G., T. Mukerji, and J. Dvorkin (2009), *The Rock Physics Handbook: Tools for Seismic Analysis of Porous Media - 2nd Edition*, 524 p., Cambridge Univ. Press, New York.
Müller, T. M., and E. Rothert (2006), Seismic attenuation due to wave-induced flow: Why Q in random structures scales differently, *Geophys. Res. Lett.*, *33*, L16305, doi:10.1029/2006GL026789.
Müller, T. M., and P. N. Sahay (2011), Porous medium acoustics of wave-induced vorticity diffusion, *Appl. Phys. Lett.*, *98*, 084,101.
Müller, T. M., B. Gurevich, and M. Lebedev (2010), Seismic wave attenuation and dispersion resulting from wave-induced flow in porous rocks - A review, *Geophysics*, *75*, 75A,147–75A,164.
Nakagawa, S., and M. A. Schoenberg (2007), Poroelastic modeling of seismic boundary conditions across a fracture, *J. Acoust. Soc. America*, *122*, 831–847.
Nelson, R. A. (2001), *Geologic Analysis of Naturally Fractured Reservoirs. Second Edition*, Gulf Professional Publishing, Boston, MA.
Payne, S. S., M. H. Worthington, N. E. Odling, and L. J. West (2007), Estimating permeability from field measurements of seismic attenuation in fractured chalk, *Geophys. Prospect.*, *55*, 643–653.
Peacock, S., C. McCann, J. Sothcott, and T. R. Astin (1994), Experimental measurements of seismic attenuation in microfractured sedimentary rock, *Geophysics*, *59*, 1342–1351.
Pride, S. R., J. G. Berryman, and J. M. Harris (2004), Seismic attenuation due to wave-induced flow, *J. Geophys. Res.*, *109*, B01201, doi:10.1029/2003JB002639.
Pyrak-Nolte, L. J., and J. P. Morris (2000), Single fractures under normal stress: The relation between fracture specific stiffness and fluid flow, *Int. J. Rock Mech. Min.*, *37*, 245–262.
Quintal, B., H. Steeb, M. Frehner, and S. M. Schmalholz (2011), Quasi-static finite element modeling of seismic attenuation and dispersion due to wave-induced fluid flow in poroelastic media, *J. Geophys. Res.*, *116*, B01201, doi:10.1029/2010JB007475.
Rubino, J. G., and K. Holliger (2013), Research note: Seismic attenuation due to wave-induced fluid flow at microscopic and mesoscopic scales, *Geophys. Prospect.*, *61*, 882–889.
Rubino, J. G., C. L. Ravazzoli, and J. E. Santos (2009), Equivalent viscoelastic solids for heterogeneous fluid-saturated porous rocks, *Geophysics*, *74*, N1–N13, doi:10.1190/1.3008544.
Rubino, J. G., D. R. Velis, and K. Holliger (2012), Permeability effects on the seismic response of gas reservoirs, *Geophys. J. Int.*, *189*, 448–468.
Rubino, J. G., L. Guarracino, T. M. Müller, and K. Holliger (2013), Do seismic waves sense fracture connectivity?, *Geophys. Res. Lett.*, *40*, 692–696, doi:10.1002/grl.50127.
Schijns, H., D. R. Schmitt, P. J. Heikkinen, and I. T. Kukkonen (2012), Seismic anisotropy in the crystalline upper crust: Observations and modelling from the Outokumpu scientific borehole, Finland, *Geophys. J. Int.*, *189*, 541–553.
Tsvankin, I. (2012), *Seismic Signatures and Analysis of Reflection Data in Anisotropic Media - Third edition*, Geophysical references series No. 19, Society of Exploration Geophysicists, Tulsa, Okla.
Varghese, A. V., M. Chapman, and J. V. Herwanger (2009), Attenuation estimation in croswell data—An indicator of fracture density and permeability?, paper presented at 71st EAGE Conference and Exhibit, Amsterdam, Netherlands.
Wenzlau, F., J. B. Altmann, and T. M. Müller (2010), Ansiotropic dispersion and attenuation due to wave-induced flow: Quasi-static finite-element modeling in poroelastic solids, *J. Geophys. Res.*, *115*, B07204, doi:10.1029/2009JB006644.